Available online at www.sciencedirect.com
SCIENCE DIRECT®
PERGAMON
International Journal of Multiphase Flow 29 (2003) 603–620
International Journal of Multiphase Flow
www.elsevier.com/locate/ijmulflow

Laminar light particle and liquid two-phase flows in a vertical pipe

R. Luo *, X.H. Pan, X.Y. Yang

Department of Thermal Engineering, Tsinghua University, Beijing 100084, PR China

Received 30 September 2002; received in revised form 26 January 2003

Abstract

Dilute laminar expanded polystyrene particle–oil flows in a vertical pipe were studied using a three-dimensional particle image tracking (PIT) method. The particle volume fraction profiles and other flow properties for the upward fully developed flows were measured. The experimental results showed that the particles in both the large and small particle and oil flows have a wall-peaked distribution similar to those of near-spherical bubbles in laminar bubbly flows. The ordered particle distribution structure consisting of particle clusters and its transition to disordered flow structures were observed. Comparisons between the bubble and particle volume fraction profiles indicate that the major difference of two-phase flow properties may result from bubble deformation.

Keywords: Particle–liquid flow; Bubbly flow; Phase distribution; 3D PIT; Wall shear stress; Bubble deformation; Lift force

1. Introduction

Dispersed flow in a pipe is a basic two-phase flow problem. To simplify its analysis, the dispersed phase is usually considered as a mass of spherical particles or bubbles. However, it is evident that particles in most real dispersed flows are not spherical and the spherical particle assumption may lead to incorrect conclusions. In particular, for laminar bubbly flows in vertical pipes, bubble size has a decisive effect on phase and velocity distributions (Nakoryakov et al., 1996; Song et al., 2001). Small bubbles approach the pipe wall and form the wall-peaked profile (Kashinsky et al., 1993). In contrast, large bubbles may tend to peak in the pipe center. One

* Corresponding author.
E-mail address: ruiluo@mail.tsinghua.edu.cn (R. Luo).

0301-9322/03/$ - see front matter
doi:10.1016/S0301-9322(03)00017-X

explanation for this difference is that the lift force on a bubble in a shear flow will change direction as the bubble becomes an ellipsoid due to its large size. Therefore the phase distribution measurement of 'bubbly' flows consisting of perfect large spherical 'bubbles' may give experimental support to this explanation.

It is an established fact that a small bubble in a liquid which is not carefully purified will dynamically behave almost like a rigid sphere of the same size in the same liquid (Rivière et al., 1999). Consequently a laminar bubbly flow may be simulated by a particle–liquid flow if the particles are light enough. Indeed, this simulation has several advantages, including perfect and uniform 'bubbles' and 'bubbles' that can also be dyed or marked for imaging measurement. However the price paid for those advantages is that the movable front surface of a bubble in even a heavily contaminated liquid (Cuenot et al., 1997) can generate a flow different from that around a solid surface. More importantly, the flow around a solid sphere can not be approximated closely by a potential flow, which can be done for bubbles with completely movable surfaces (Spelt and Sangani, 1998). Also, the deformation of bubbles near the pipe wall may have an important effect on the motion of the bubbles.

Alajbegovic et al. (1994) performed phase and velocity distribution measurements for dilute expanded polystyrene particle–water two-phase flows. Their results showed that the phase and velocity distributions for the turbulent light particles–water flows are very similar to those for bubbly water flows. In this study, the phase distributions for expanded polystyrene particle–oil flows are measured using the particle image tracking (PIT) technique, and the results are compared with those for real bubbly flows.

2. Experimental methods and apparatus

2.1. Test loop

A solid–liquid two-phase loop was constructed to conduct the experiments. The loop was an 'O' closed loop, in which the solid–liquid flow was confined, as shown in Fig. 1. A vertical pipe of 29 mm ID was used as the test section and the downcomer had a 26 mm ID. The pressure drop, ΔP_{AB}, between points A and B on the test section was measured by a pair of pressure tapes. An orifice was mounted near the bottom of the downcomer to obtain the solid–liquid mixture's liquid flow rate, Q_3. There was a nozzle at the top of the vertical pipe through which liquid was injected into the closed loop to circulate the solid–liquid mixture. Liquid without particles could flow out of the closed loop at the top and bottom of the vertical pipe. The liquid flow rates both into and out of the closed loop at the top, Q_1 and Q_2, were measured by two flow meters which were calibrated for each reading of all test runs at the working temperature for uncertainty less than 3%.

Mineral oil was used as the liquid phase. A cooling system controlled the liquid temperature at 25 ± 0.3 °C during the experiments. The liquid density, ρ_L, at 25 °C was 870 kg/m^3, and the dynamic viscosity, μ_L, was 0.0175 Pa s. Two sizes of expanded polystyrene particles were used as the dispersed phase. The larger particles had a mean diameter of 5.47 mm with more than 95% of the particles having diameters within 5.3–5.7 mm. The small particles had a mean diameter of 3.1 mm with more than 95% of the particles having diameters within 2.8–3.2 mm. Both large and small particles had a density of 30 kg/m^3, ρ_P.

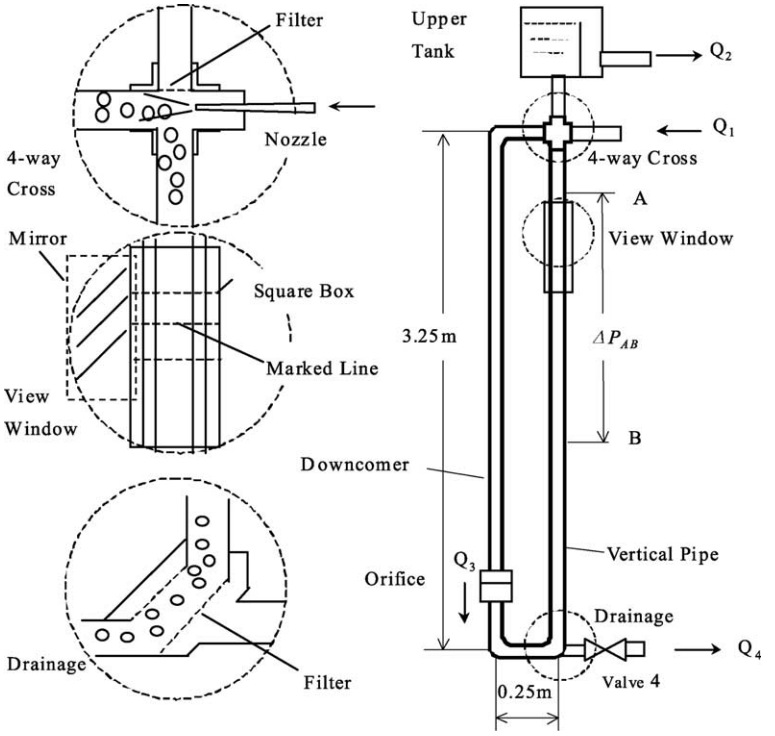

Fig. 1. Experimental loop (not to scale).

2.2. Generation of the particle–liquid two-phase flow

Since the expanded polystyrene particles were fragile and could be deformed or even ruptured easily by a machinery pump, the particle–liquid mixture could not be circulated with an ordinary pump. Therefore a special method was designed to drive the particle–oil flows. A 4-way cross was located at the top of the upward pipe, as shown in Fig. 1. The particle–liquid flow entered through the lower opening of the cross and exited through its left opening. The opening at the top of the cross allowed liquid to flow out, but there was a filter blocking the particles. Single-phase liquid was injected, at a high velocity into the 4-way cross from its right-hand side which entrained the particles into the downcomer. Then the high-speed liquid decelerated and transfered kinetic energy into the pressure head of the particle–liquid mixture in the downcomer. The mixture was driven by the pressure head to circulate in the 'O' closed loop. Although similar to a jet pump, this pump worked at low Reynolds number flow conditions and had a low efficiency approaching zero. As a result, the liquid flow rate in the downcomer, Q_3, would be close to the liquid flow rate injected into the closed loop, Q_1.

The liquid from the downcomer could be drained from the bottom of the vertical pipe to adjust the liquid flow rate into the test section. Also, the mean particle phase fraction in the test section could be regulated by changing the injected liquid flow rate, Q_1, and the drainage, $Q_4 = Q_1 - Q_2$. For example, if both Q_1 and Q_4 were increased, the mixture velocity in the downcomer would increase while the velocity in the test section would remain constant or even decrease. As a result,

the number of particles in the vertical pipe increased because the higher velocity liquid from the downcomer transported more particles into the vertical pipe. Finally the particle phase fraction in the test section rose.

It should be noted that the particles were put in the 'O' closed loop before the tests and the amount of particles, which was known beforehand, was maintained during experiments. No container or pipe section had a diameter considerably larger than that of the downcomer or the vertical pipe. Therefore the total volume of all particles in the closed loop was:

$$V_P = \overline{\varepsilon_D} A_D L_D + \overline{\varepsilon_P} A_U L_U + \overline{\varepsilon_H} A_D L_H = \text{constant} \tag{1}$$

where $\overline{\varepsilon_D}, \overline{\varepsilon_P}, \overline{\varepsilon_H}$ are the mean particle volume fraction in the downcomer, the vertical pipe, and the horizontal connections between them. A and L are the corresponding inner cross-sectional area and length of the pipes, as shown in Fig. 1. The mean particle volume fraction of the vertical pipe was obtained using the three-dimensional PIT technique. Then $\overline{\varepsilon_H}$ was estimated as:

$$\overline{\varepsilon_H} = \frac{1}{2}(\overline{\varepsilon_P} + \overline{\varepsilon_D}) \tag{2}$$

Finally the mean particle volume fraction in the downcomer was obtained from the given V_P and $\overline{\varepsilon_P}$. Here the mean particle volume fraction in the whole vertical pipe was approximately equal to that in the test section.

2.3. Liquid and particle flow rate measurements

It is difficult to measure the liquid flow rate in particle–oil flows through the test section using an ordinary single-phase flow meter. An electro-magnetic flowmeter, which was used to measure the liquid flow rate of particle–water flows by Alajbegovic et al. (1994), also is not applicable to the present oil–particle flows due to the non-conductivity of the oil. So an orifice was used to measure the liquid flow rate through the downcomer. The relationships among all liquid flow rates may be written as:

$$Q_3 = Q_T + Q_4 \tag{3}$$

$$Q_1 = Q_2 + Q_4 \tag{4}$$

where Q_T is the liquid flow rate through the test section.

The orifice was only calibrated for single-phase liquid flows. But for the tests here, it was used for dispersed two-phase flows; therefore a suitable model had to be applied to obtain the single-phase liquid flow rate from the measured two-phase flow rate of the particle–liquid mixture. The volume flow rate of the two-phase mixture through the orifice can be related to the pressure drop over it as:

$$Q_{TP} = A\left(\frac{\Delta P_{TP}}{\rho_{TP}}\right)^n \tag{5}$$

where ρ_{TP} is the density of the two-phase mixture. For dilute dispersed two-phase flows, it can be estimated as:

$$\rho_{TP} = \rho_L(1 - \overline{\varepsilon_D}) + \rho_P\overline{\varepsilon_D} \approx \rho_L(1 - \overline{\varepsilon_D}) \tag{6}$$

leading to the liquid flow rate:

$$Q_3 = (1 - \overline{\varepsilon_D})Q_{TP} = (1 - \overline{\varepsilon_D})^{(1-n)} C \left(\frac{\Delta P_{TP}}{\rho_L} \right)^n = (1 - \overline{\varepsilon_D})^{(1-n)} Q_{L_0} \tag{7}$$

where C and n are constants that were obtained by calibration with single-phase liquid flows, Q_{L_0} is the volume flow rate if the mixture flow is regarded as a single-phase liquid flow. For the present orifice and liquid phase, $n = 0.54$.

The particle phase flux in the test section was determined by measurement of the mean particle velocity, $\overline{U_P}$, and particle phase fraction, $\overline{\varepsilon_P}$. The measurement method will be discussed later in detail.

2.4. Friction pressure drop of particle–liquid flows

For fully developed laminar particle–liquid flows, the pressure balance on the test section between points A and B as shown in Fig. 1 gives:

$$\Delta P_{AB} = \Delta P_f - \Delta P_B \tag{8}$$

where ΔP_{AB}, ΔP_f, and ΔP_B are the overall pressure difference relative to the hydro-static pressure difference, the friction pressure drop, and the buoyancy pressure head induced by the particles between A and B. Then

$$\Delta P_f = \Delta P_{AB} + \overline{\varepsilon_P} L_{AB} (\rho_L - \rho_P) g \tag{9}$$

where L_{AB} is the pipe length between A and B.

For the single-phase Poiseuille flow at the same mean volumetric flow rate as the particle–oil mixture, the friction pressure drop is calculated as (Rivière et al., 1999):

$$\Delta P_{f_0} = 8\mu_L L_{AB} \frac{1}{R^2} \left[\frac{U_{SL}}{(1 - \overline{\varepsilon_P})} \right] \tag{10}$$

where R is the pipe radius and the term in square brackets is the mean liquid velocity of the single-phase flow. Accordingly the measured ratio of the wall shear stress of the two-phase flow to that of the single-phase flow can be written as:

$$\frac{\tau_{WTP}}{\tau_{W_0}} = \frac{\Delta P_f}{\Delta P_{f_0}} = \frac{\Delta P_{AB}/L_{AB} + \overline{\varepsilon_P}(\rho_L - \rho_P) g}{8\mu_L \frac{1}{R^2} \left[\frac{U_{SL}}{(1 - \overline{\varepsilon_P})} \right]} \tag{11}$$

2.5. Three-dimensional photographic method for measurement of particle velocity and phase distributions

A previously developed three-dimensional photographic method (Song et al., 2001) has been updated to a digital image processing system to measure the particle phase and velocity distributions. The basic methodology was unchanged, i.e. a mirror was used to reflect a side view of the flow to the front view direction and then flow images from both the side and front views were taken by one CCD camera. The flow images were digitalized in real time by an image grabber and

stored on a PC. The images were then processed by a set of software developed to identify and locate the particles on both the side and front view images.

Since the particles were perfect spheres and were dyed black, flow images appeared as groups of uniform black disks with a gray background, as shown in Fig. 2. It would be easy to treat this kind image by the image processing software. As a result, the 2D coordinates of each particle center on both the front and side view images could be determined at an accuracy of one or two pixels. Then the spatial position of each particle was determined by matching its front view image to its side view image. A detailed description of the PIT technique is given in Pan et al. (2002).

The matching of front and side view images can results in over 10% re-matched or mis-matched particles (Song et al., 2001; Luo et al., 2002; Pan et al., 2002). Those re-matched or mis-matched particles were removed in the present study, and only correctly matched particles were used to determine the phase distribution. Finally, the particle volume fraction profile was modified by multiplying the ratio of the total particle number to the correctly matched particle number.

The particle velocity could be obtained by precisely tracking each particle because the particle number density was small and the particle velocity fluctuation was negligible in the dilute laminar particle–liquid flows studied here.

2.6. Error analysis

The liquid flow rate through the test section, Q_T, was measured at the orifice, which was calibrated with single-phase liquid flow at each reading. Its relative error could be estimated to be less than 5% due to the applications limited to the dispersed flows at small mean particle volume fractions (less than 10%). However, since the liquid flow rates for low velocity flows, as in Tests L9, L10, S9, and S10 (see Table 1 later), result from the subtraction between two large flow rates, Q_3 and Q_4, in Eq. (3), they might have a relative error up to 15–20%.

Another error source is from the particle volume fraction measured by PIT. Some of the flow parameters depend on it, including the liquid flow rate and the wall shear stress. In particular, the measured mean particle volume fraction is a decisive factor in estimating the wall shear stress from the measured overall pressure drop. Obviously the measurement of particle phase distribution is one of the main tasks in the present study. The re-matched or mis-matched particles have been removed, and no longer affect the measurement accuracy. In addition, the particles could keep their spherical shapes and, then, their volumes during flow. So only the total number of particles is important to determine both the mean particle volume fraction and its distribution. Typically only one or two particles in the measurement zone of each field image could not detected by the image processing software. The total number of particles in one field image was 30–40. For some denser flows, the undetetected particle number rose, at most, to 3–4 of the total particles of about 50 since the particle images overlapped each other. So the particle volume fraction measurement should have better than 10% accuracy for all the tests (Pan et al., 2002).

2.7. Experimental procedures

At the start, a liquid flow was injected at high speed into the 4-way cross through the nozzle to drive the particle–liquid mixture in the 'O' loop at a high velocity. In addition, valve 4 was closed to prevent the particles conglomerating on the filter of the drainage. After the particles were

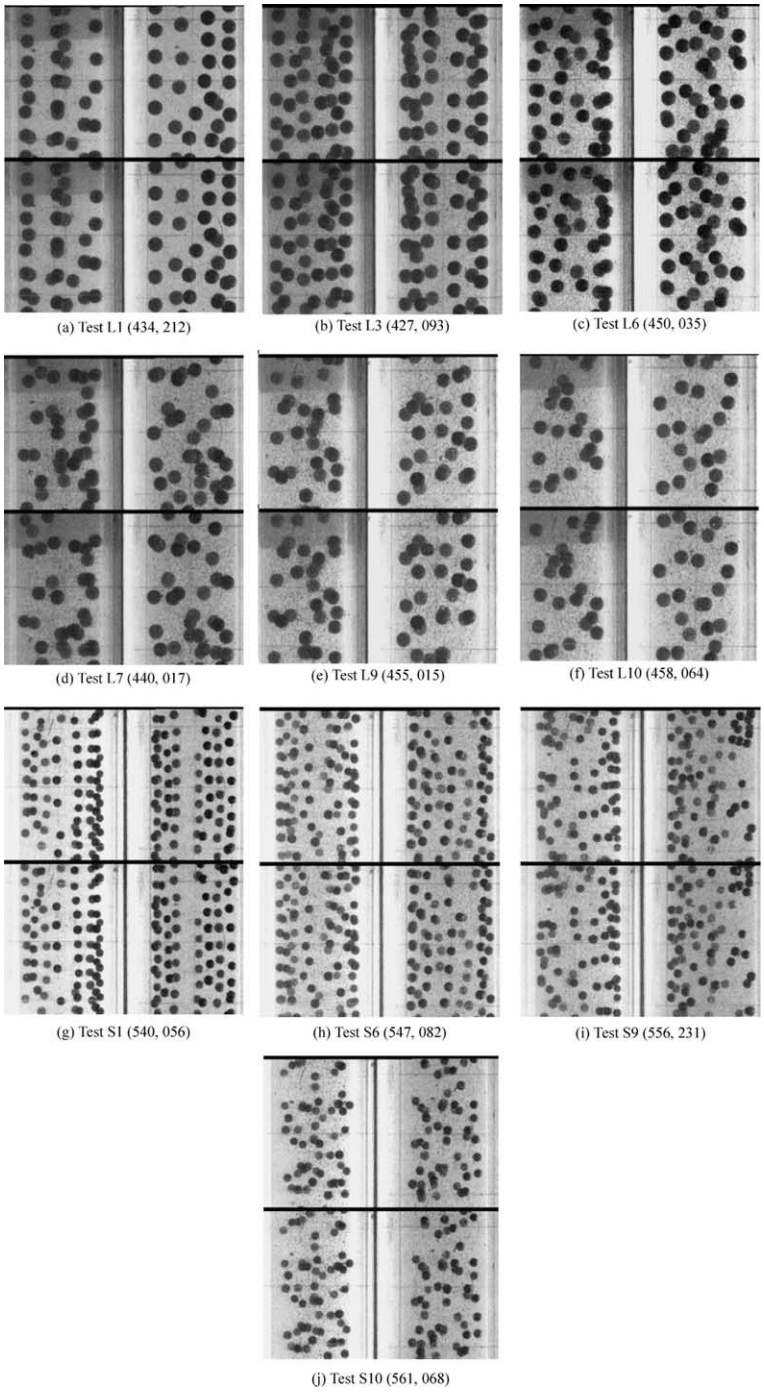

Fig. 2. Side view (left) and front view (right) images for two successive fields (time interval = 0.02 s). The first number in the brackets is the original image file number, and the second is the frame number. (a) Test L1 (434, 212), (b) Test L3 (427, 093), (c) Test L6 (450, 035), (d) Test L7 (440, 017), (e) Test L9 (455, 015), (f) Test L10 (458, 064), (g) Test S1 (540, 056), (h) Test S6 (547, 082), (i) Test S9 (556, 231), and (j)Test S10 (561, 068).

completely dispersed in the closed loop to reach a uniform distribution along the vertical pipe and downcomer, the liquid flow rates into and out of the closed loop were adjusted slowly to the desired values.

Measurements were performed after the particle–liquid flow reached steady. For most flow runs, the images of the flow were taken three times, and each image recording took about 9.4 s. So a 28.2-s image for each test was obtained. During the intervals between the image recording, the readings of all flow rates and pressure drops were noted.

3. Results and discussion

Twenty tests were performed in total, 10 for small particles and 10 for large particles. All flow conditions and parameters are summarized in Table 1. Some previous experiment results of real bubbly flows by several investigators are listed in Table 2 for comparisons with the particle–liquid flows. The number in the brackets of the first column is the original image file number in Table 1. The flow rates listed in the tables have been defined in Sections 2.1–2.3. The overall pressure difference, ΔP_{AB}, between A and B in Fig. 1 has been expressed as a value relative to the static liquid pressure difference. The Poiseuille number, P, the pipe Reynolds number, Re_D, and the bubble Reynolds number, Re_b, in Table 1 are defined as $P = (\mu_L U_{SL})/(g\rho_L D_P^2)$, $Re_D = (\rho_L U_{SL} D_P)/\mu_L$, and $Re_b = (\rho_L U_r 2R_b)/\mu_L$, where $D_P = 2R$, U_{SL}, R_b, and U_r are the pipe ID, the superficial liquid velocity, the bubble radius, and the bubble rise velocity in the quiescent liquid.

Another important parameter is the ratio of the particle or bubble radius to the pipe radius, R_b/R. It is 0.186 for large particles and 0.107 for small particles. The 'bubble' Reynolds number, Re_b, is about 62 for large particle flows and about 19 for small particle flows. The equivalent superficial particle phase velocity, U_{SG}, in Table 1 is estimated with $U_{SG} = \overline{U_P} \cdot \overline{\varepsilon_P}$ for a better comparison with real bubbly flows. β is naturally defined as $\beta = U_{SG}/(U_{SL} + U_{SG})$. In addition, the dimensionless shear rate of the liquid phase is $\alpha' = 4(U_{SL}/U_r)(R_b/R)$ (Kurose and Komori, 1999), where the liquid velocity gradient is calculated at the pipe wall in the single-phase Poiseuille flow with mean velocity being equal to U_{SL}.

3.1. Observations of particle–liquid flows

For all the tests, under all flow conditions, regardless of whether the flows were large or small particle flows or were at low or high velocity, the particles always tended to peak near the pipe wall. No center-peaked particle phase distribution was observed. However, for flows with a liquid superficial velocity smaller than a specific value, the particle distribution peak shifted towards the pipe center as the liquid velocity decreased. For large particle flows, this value was 0.24 m/s, and for small particles, it was 0.15 m/s. In addition, if liquid velocity was low, more particles scattered in the pipe center region.

For high velocity flows, the particles not only aggregated in an annulus close to the pipe wall but also tended to line up and form clusters, Fig. 2(a) and (b). This is very similar to what has previously been observed in laminar bubbly flows (Song et al., 2001). But unlike the bubbles in laminar bubbly flows which have a linear and stable motion without contacting the pipe wall, the

Table 1
Properties of the expanded polystyrene particle–oil two-phase flows

Test No.	Q_1 (l/s) Exp.	Q_2 (l/s) Exp.	Q_{L_0} (l/s) Exp.	Q_3 (l/s) Eq. (7)	Q_T (l/s) Eq. (3)	U_{SL} (m/s)	$\overline{U_P}$ (m/s) Exp.	P (10^{-3})	U_{SG}[a] m/s	β	Re_D	α'	$\Delta P_{AB}/L_{AB}$ (Pa/m) Exp.	$\overline{\varepsilon_P}$ (%) Exp.	$\overline{\varepsilon_D}$ (%) Eq. (1)	$\Delta P_f/L_{AB}$ (Pa/m) Eq. (9)	$\frac{\tau_{WTP}}{\tau_{W_0}}$ Eq. (11)
L1(434-6)[b]	0.354	0.354	0.316	0.309	0.309	0.476	0.366	1.16	0.022	0.045	682	1.52	256	6.08	5.33	757	2.24
L2(431-3)	0.296	0.296	0.215	0.210	0.210	0.323	0.274	0.79	0.015	0.044	462	1.03	143	5.42	6.17	589	2.89
L3(427-9)	0.354	0.102	0.444	0.441	0.189	0.291	0.263	0.71	0.024	0.076	417	0.93	59.1	9.11	1.59	809	3.76
L4(447-9)	0.354	0.059	0.470	0.467	0.172	0.265	0.254	0.65	0.023	0.079	380	0.84	18.8	8.97	1.76	757	3.86
L5(437-9)	0.296	0.116	0.342	0.336	0.156	0.240	0.243	0.59	0.016	0.064	344	0.76	38.4	6.70	4.62	590	3.44
L6(450/4)	0.354	0.032	0.480	0.475	0.153	0.236	0.245	0.58	0.020	0.080	338	0.75	−51.1	8.34	2.55	635	3.74
L7(440-2)	0.296	0.055	0.377	0.370	0.129	0.199	0.279	0.49	0.018	0.085	285	0.63	−101	6.59	4.71	441	3.11
L8(443-5)	0.296	0.018	0.403	0.395	0.117	0.180	0.305	0.44	0.021	0.102	258	0.57	−198	6.75	4.52	358	2.78
L9(455-6)	0.261	0.013	0.325	0.317	0.069	0.106	0.285	0.26	0.016	0.134	152	0.33	−239	5.77	5.75	236	3.54
L10(458/60)	0.235	0.003	0.295	0.286	0.054	0.083	0.269	0.20	0.012	0.127	119	0.26	−310	4.47	7.22	58.0	1.01
S1(540-2)	0.354	0.220	0.435	0.430	0.296	0.456	0.222	1.12	0.0063	0.0136	653	1.57	266	2.83	2.59	499	1.59
S2(534-6)	0.296	0.296	0.296	0.290	0.290	0.447	0.223	1.10	0.0059	0.0130	640	1.54	223	2.63	2.86	440	1.44
S3(553-5)	0.296	0.231	0.320	0.315	0.250	0.385	0.193	0.94	0.0047	0.0120	552	1.32	228	2.42	3.12	427	1.62
S4(537-9)	0.238	0.238	0.220	0.216	0.216	0.333	0.176	0.82	0.0033	0.0098	477	1.15	145	1.87	3.84	299	1.32
S5(543-5)	0.354	0.092	0.465	0.460	0.198	0.305	0.168	0.75	0.0049	0.0158	437	1.05	119	2.91	2.50	359	1.71
S6(547-9)	0.354	0.001	0.490	0.484	0.131	0.202	0.122	0.50	0.0029	0.0142	289	0.69	34.1	2.39	3.15	231	1.68
S7(558-0)	0.215	0.096	0.230	0.227	0.108	0.166	0.112	0.41	0.0026	0.0156	238	0.57	0	2.35	3.11	193	1.69
S8(550-2)	0.296	0.021	0.384	0.378	0.103	0.158	0.112	0.39	0.0023	0.0145	226	0.54	17.1	2.07	3.50	188	1.75
S9(556/7)	0.261	0.025	0.330	0.325	0.089	0.137	0.113	0.37	0.0021	0.0152	196	0.47	−17.1	1.87	3.84	137	1.47
S10(561-3)	0.215	0.001	0.278	0.272	0.057	0.088	0.140	0.22	0.0020	0.0225	126	0.30	−19.8	1.45	4.02	98	1.62

[a] The equivalent superficial gas velocity is estimated with $U_{SG} = \overline{U_P} \cdot \overline{\varepsilon_P}$.

[b] The first letter, L, stands for large particles; S is for small particles. The numbers in brackets in the first column are the original image file codes of the tests.

Table 2
Properties of real bubbly flows in a few experimental investigations

Data source	Data code	ν_L (10^{-6} m^2/s)	D_P (mm)	ρ_L (kg/m^3)	R_b (mm)	$2R_b/D_P$	U_{SL} (m/s)	U_{SG} (m/s)	P (10^{-3})	β	Re_D	Re_b	α'	$\overline{\varepsilon_b}$	$\frac{\tau_{WTP}}{\tau_{W_0}}$
Kashinsky et al. (1993)	KA(M)1[a]	7.02	14.8	1140	0.3	0.04	0.32	0.0035	1.04	0.01	674	50.6	0.09		0.98
	KA(M)2	7.02	14.8	1140	0.55	0.074	0.16	0.0084	0.52	0.05	338	50.6	0.15		0.9
	KA(M)3	7.02	14.8	1140	0.65	0.087	0.32	0.017	1.04	0.05	674	55.2	0.37		1.06
	KA(P)4	7.02	14.8	1140	1.05	0.141	0.32	0.0032	1.04	0.01	674	41.6	1.29		1.11
	KA(P)5	7.02	14.8	1140	1.25	0.168	0.32	0.017	1.04	0.05	674	59.6	1.28		1.2
Nakoryakov et al. (1996)	NA(P)1	3.5	14.8	1127	1.1	0.148	0.207	0.023	0.33	0.1	876	116	0.66	0.05	
	NA(P)2	3.5	14.8	1127	1.0	0.135	0.44	0.049	0.71	0.1	1862	94.4	1.44	0.069	
	NA(N)3	3.5	14.8	1127	1.85	0.25	0.44	0.049	0.71	0.1	1862	318	1.46	0.055	
Rivière et al. (1999)	RI(P)1	10	14.8	1169	0.65	0.087	0.663	0.0135	3.08	0.02	980	9.6	3.09		1.09
	RI(P)2	10	14.8	1169	1.05	0.141	0.072	0.008	0.33	0.1	108	25.4	0.34		0.45
	RI(P)3	10	14.8	1169	1.2	0.162	0.203	0.0228	0.94	0.1	300	34.2	0.92		1.03
	RI(P)4	10	14.8	1169	1.15	0.155	0.38	0.0442	1.77	0.1	562	31.2	1.73		1.1
	RI(M)5	10	14.8	1169	0.6	0.081	0.0135	0.0015	0.06	0.1	20	6.6	0.08		−1.30
	RI(M)6	10	14.8	1169	0.5	0.067	0.0324	0.0036	0.15	0.1	48	4	0.22		0.95
	RI(M)7	10	14.8	1169	0.7	0.094	0.203	0.0041	0.94	0.02	300	12	0.88		1.40
	RI(M)8	10	14.8	1169	0.65	0.087	0.38	0.0078	1.77	0.02	562	9.6	1.77		1.10
Song et al. (2001)	SO1	35.6	29	866	1.5	0.103	0.27	0.0082	1.16	0.03	186	9.3	0.84	0.013	
	SO2	35.6	29	866	1.65	0.113	0.20	0.0082	0.86	0.04	138	12	0.58	0.017	
	SO3	35.6	29	866	1.6	0.11	0.13	0.0082	0.56	0.06	90	11.1	0.39	0.019	
	SO4	35.6	29	866	1.65	0.113	0.08	0.0082	0.34	0.09	56	12	0.24	0.02	
	SO5	35.6	29	866	1.2	0.082	0.27	0.0048	1.16	0.017	186	5.4	0.92	0.015	
	SO6	35.6	29	866	1.35	0.093	0.20	0.0048	0.86	0.023	138	7.2	0.66	0.021	
	SO7	35.6	29	866	1.35	0.093	0.13	0.003	0.56	0.023	90	7.2	0.43	0.018	
	SO8	35.6	29	866	1.4	0.096	0.08	0.003	0.34	0.036	56	7.8	0.26	0.016	

[a] M in brackets stands for the type of gas injector, see reference.

particles near the pipe wall periodically slid and collided with the pipe wall. The particles rotated at a frequency of about 2–3 Hz.

As the liquid velocity decreased, the clusters became more unstable and most likely to disperse although most of the particles still accumulated in an annulus near the pipe wall, Fig. 2(c) and (d). In addition, the particles in low velocity flows did not usually collide with the pipe wall, Fig. 2(e) and (f). In this case, the particles tended to distribute more randomly over the pipe cross section.

The particles rarely collided with each other in all the tests. For high velocity flows, most of the particles aggregated in an annulus close to the pipe wall and formed clusters. Pairs of particles in the clusters had an almost fixed distance beyond which they could not approach each. Although particles in low velocity flows might be distributed randomly in the pipe, the Bernoulli effect between two adjacent particles in different radial positions, which drives two particles to approach each other, was depressed by the main flow shear. As a result, these two particles tended to keep a linear motion and would not get closer to each other. In addition, even for low velocity flows, there were fewer particles in the pipe center region resulting in a reduced possibility of particle collision.

3.2. Particle volume fraction profiles

Fig. 3 shows the measured particle volume fraction profiles in the radial direction. $r/R = 1$ denotes the pipe wall. A particle volume fraction profile for each image measurement is given respectively. For most test runs the difference between two measurements is small. Typically, each measurement for a middle particle volume fraction flow involves about 2000 particles.

All particle fraction profiles are wall-peaked, although the particle size is very large. Actually, for the flow at a superficial liquid velocity higher than 0.24 m/s for large particle tests, the lift force induced by the liquid shear flow was so strong that the particles periodically collided with the pipe wall. As a result, most particles in higher velocity flows continued to intermittently contact with the pipe wall. Integrating all the information from particles colliding with the pipe wall gives the major peak of the particle volume fraction profile, Fig. 3(a)–(h). The peak base has a width almost equal to the particle diameter, and the distance between the peak tip and the pipe wall is half of the particle diameter.

This can be seen more clearly when all particle center positions are shown on a cross section of the pipe, Figs. 4 and 6. Fig. 4(a) and (b) show that the centers of most particles in Tests L1 and L2 are located precisely on an annulus. As the liquid velocity decreases and the lift force becomes weaker, more particles shift to the pipe center due to the wall force, Fig. 4(c)–(f). In this situation, most particles no longer collide with the pipe wall. Fig. 4 also shows that the particles have a uniform distribution in the azimuthal direction of pipe. However, it should be noted that there is a slight asymmetry of particle distributions due to the error of the image measurement system and the optical deformation of the circular pipe wall. This geometric error gives rise to non-zero particle volume fractions at the pipe wall as shown in Figs. 3 and 5.

Some void fraction profiles for real bubbly flows are also given in Fig. 3 for direct comparison with the particle volume fraction profiles. A remarkable difference in phase distribution is that the bubble volume fraction profile peak is farther from the pipe wall as shown in Fig. 3(a), although bubbly flows KA(P)5 and RI(P)4 have Poiseuille numbers, P, pipe Reynolds numbers, Re_D, and bubble Reynolds numbers, Re_b, close to those of Tests L1 and L2 but with slightly smaller ratios

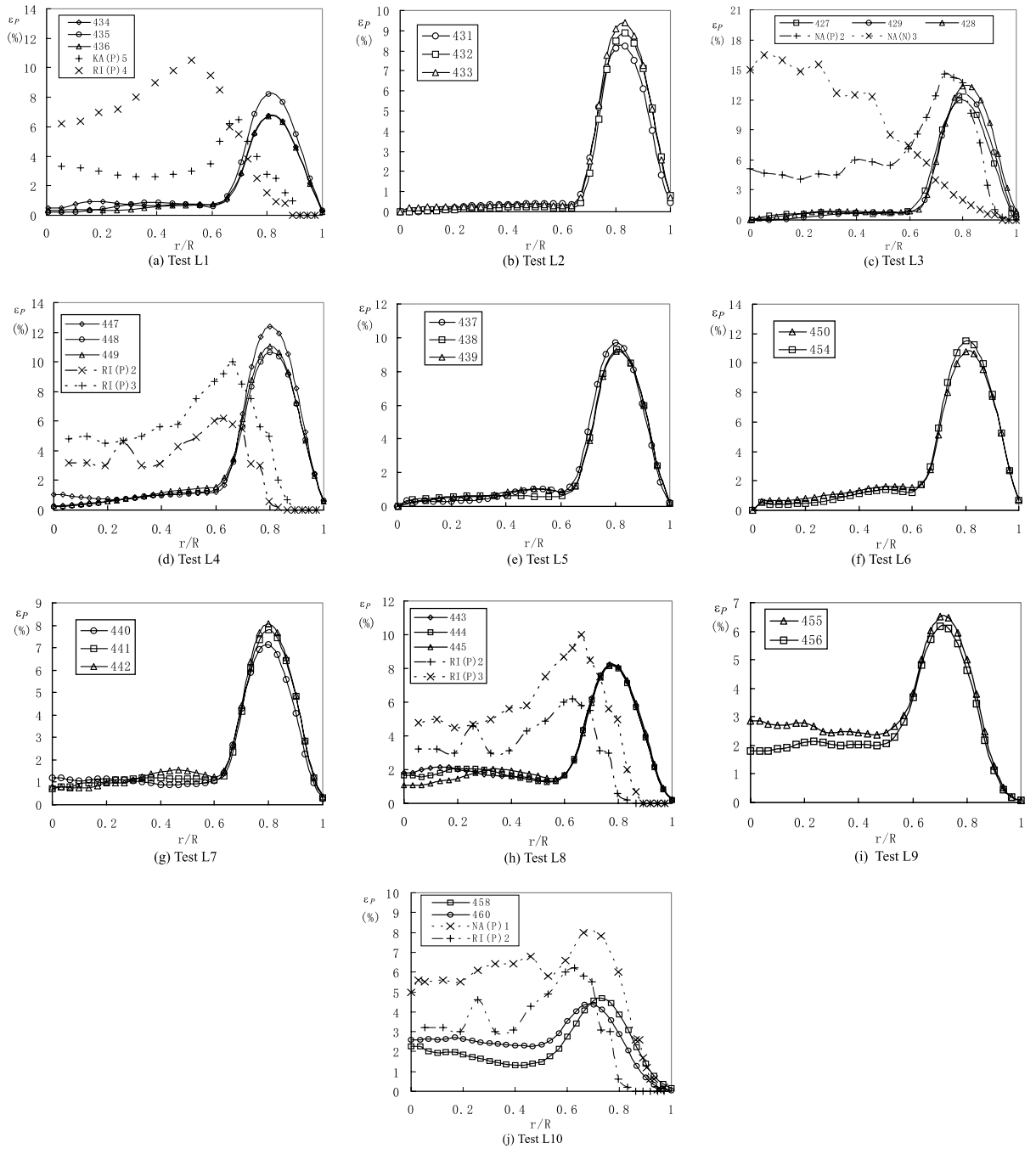

Fig. 3. Particle volume fraction profiles for large particle flows in comparison with data of real bubbly flows. The numbers or codes corresponding to the symbols in the figures are the original image file numbers, Table 1, or data codes, Table 2. (a) Test L1, (b) Test L2, (c) Test L3, (d) Test L4, (e) Test L5, (f) Test L6, (g) Test L7, (h) Test L8, (i) Test L9, and (j) Test L10.

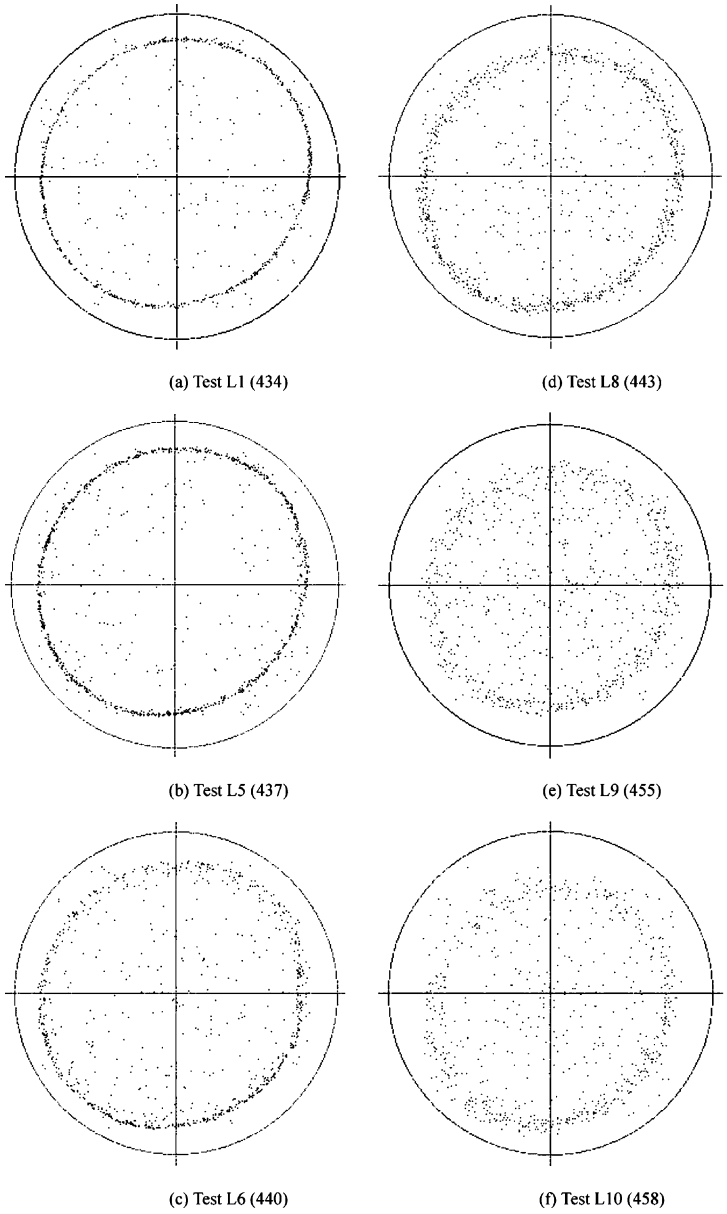

Fig. 4. Particle center number density distributions over the pipe cross-section for large particle flows. (a) Test L1 (434), (b) Test L5 (437), (c) Test L6 (440), (d) Test L8 (443), (e) Test L9 (455), and (f) Test L10 (458).

of bubble diameter to pipe I.D. As bubble size increases, the bubble volume fraction profile peak even shifts to the pipe center as shown in Fig. 3(c). This indicates that the deformation of bubbles induced by the hydrostatic pressure and liquid shear may generate a smaller lift force and a larger wall repulsion force, which is also a lubrication force, on the bubbles. The numerical simulations (Ervin and Tryggvason, 1997) and the experiments (Tomiyama et al., 2002) of a gas bubble

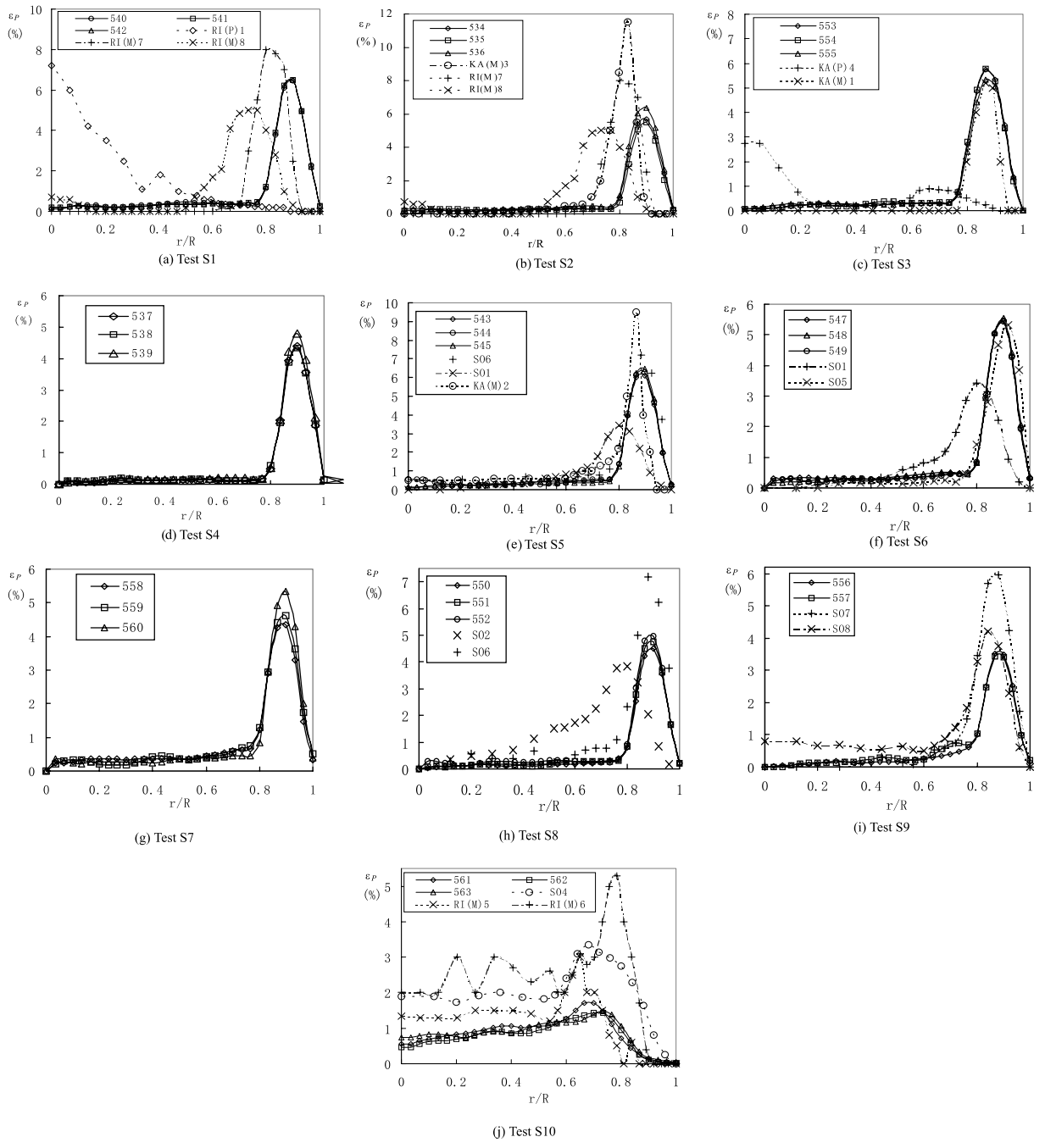

Fig. 5. Particle volume fraction profiles for small particle flows in comparison with data of real bubbly flows. The numbers or codes corresponding to the symbols in the figures are the original image file numbers, Table 1, or data codes, Table 2. (a) Test S1, (b) Test S2, (c) Test S3, (d) Test S4, (e) Test S5, (f) Test S6, (g) Test S7, (h) Test S8, (i) Test S9, and (j) Test S10.

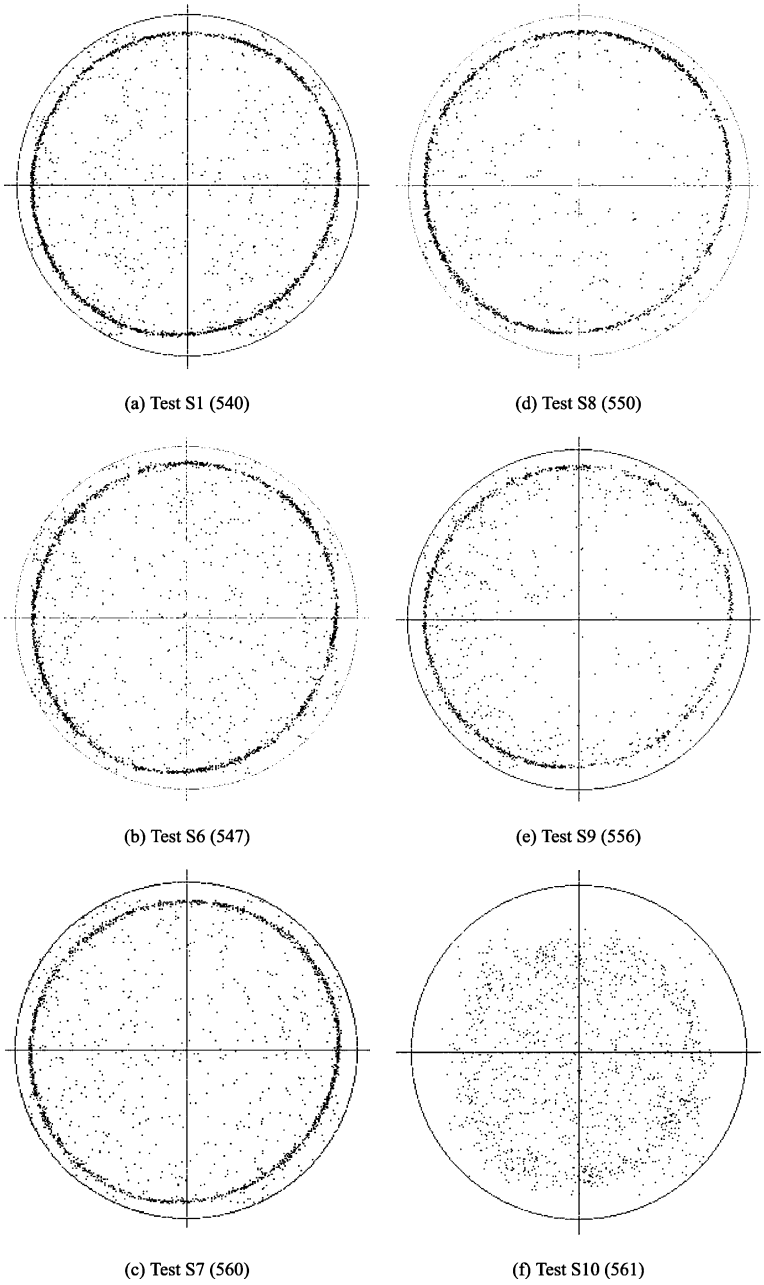

Fig. 6. Particle center number density distributions over the pipe cross-section for small particle flows. (a) Test S1 (540), (b) Test S6 (547), (c) Test S7 (560), (d) Test S8 (550), (e) Test S9 (556), and (f) Test S10 (561).

moving in a linear shear flow show that a deformed bubble may experience a 'negative' lift force, i.e. the lift force drives the bubble to migrate to the higher-liquid-velocity side. If a bubble rising in a shear flow with the velocity gradient smaller than 8–10 s^{-1} has a diameter larger than 5–5.4 mm

in water or water–glycerol solution (Lucas et al., 2001; Tomiyama et al., 2002) or 4 mm in machine oil (Song et al., 2001), the lift force on the bubble is 'negative'. In both these cases, the bubbles have the same dimensionless deformation of $E = 0.68 - 0.69$, where $E = b/a$, and a and b are the semi-major and semi-minor axes of the deformed bubble. It should be noted that the dimensionless shear rate, α', is always large for those bubbly flows with the void fraction profiles considerably different from the particle volume fraction profiles for the particle liquid flows studied here (see Table 2). Therefore, smaller bubbles in those rapid shear flows may also have a considerable deformation.

Unlike the particles in the present experiments, bubbles in bubbly flows can not contact the pipe wall even in a high velocity flow due to the smaller lift force or stronger wall repulsion force. In fact, there is a zone near the pipe wall with a vanishing bubble volume fraction as shown in Fig. 3. One probable explanation for this is that the deformation of the bubbles near the wall generates a strong wall repulsion force pushing the bubbles away from the pipe wall. However, as liquid velocity decreases, the bubble distribution is similar to the particle distribution in Fig. 3(j). Although the bubble volume fraction profiles for bubbly flows are very similar to the particle volume fraction profiles measured in the present study, the distance between the bubble profile peak and the pipe wall is about one bubble diameter (Kashinsky et al., 1993; Rivière et al., 1999). This is in contrast to the distance of a half particle diameter for particle liquid flows as mentioned before. It indicates that there is a remarkable difference in near wall flow structure between real bubbly flows and particle–liquid flows.

In a way very similar to large particle flows, the particles in small particle flows also have wall-peaked distributions as shown in Fig. 5. Since bubbles in most real bubbly flow experiments are smaller than 3.5 mm, more bubble volume fraction profiles are compared with those for small particle flows. For bubbly flows containing very small bubbles or at relatively low velocities as in flows KA(M)1, SO4-8, and RI(M)5, the bubble volume fraction profiles is nearly identical to the particle volume fraction profiles, as shown in Fig. 5(c), (f), (h), (i), and (j), except that their amplitudes may be different due to different gas flow rate ratio, β. This implies that spherical bubbles may have the same dynamic and kinetic behaviours as the particles, since very small size bubbles or bubbles without a strong shear action will keep their spherical shapes.

For low velocity flows, if liquid velocity increases, the bubbles tend to move towards the pipe wall and form the sharp bubble volume profile peak near the pipe wall due to increasing lift force, such as in flows SO2, 4, 6–8 and flows RI(M)5–7 shown in Fig. 5(b), (g), (i) and (j).

However, for higher velocity flows where small bubbles can have a nearly spherical shape even under shear action, a slight deformation may significantly alter the lift force or the wall repulsion force on the bubbles. For example, the bubbles in flows RI(M)7 and 8 have diameters of 1.3 and 1.4 mm, and should have a nearly spherical shape. But these high velocity flows have a very different feature from low velocity flows: as liquid velocity increases further, the bubble volume fraction profile peak shifts back towards the pipe center (Rivière et al., 1999), as shown in Fig. 5(a). This may be explained by the fact that the lift force on a slightly deformed bubble will decrease with the liquid shear if the liquid velocity gradient is large enough (Sankaranarayanan and Sundaresan, 2002). As the velocity gradient increases, the threshold of the dimensionless deformation E at which the lift force changes its direction will decrease. Kariyasaki (1987) experimentally found that a near-spherical bubble with E of 0.89–0.90 has a 'negative' lift fore in rapid shear flows with the dimensionless shear rate of $\alpha' \sim 2$.

In the present experiments, the shift of particle volume fraction profile peak back towards the pipe center was not observed because the deformation of the particles was negligible in comparison with that of bubbles. In addition, the rotation of particles in high velocity flows might generate a stronger lift force due to the Magnus effect (Oesterlè and Bui Dinh, 1998; Bagchi and Balachandar, 2002), which pushed the particles colliding with the pipe wall as mentioned before. Furthermore, the rotation significantly decreased the relative velocity between the particle surface and the pipe wall, and the wall repulsion force on particles decreased accordingly. These may give an explanation for that the particles and real bubbles in high velocity flows have a different distribution particularly in the region near the pipe wall.

3.3. Wall shear stress

The particle phase peak near the pipe wall produces a considerably higher wall shear stress in comparison with that in the single-phase Poiseuille flow, Table 1, and even higher than that in the bubbly flow with almost the same void fraction profile, Table 2. The reason for this is that the particle volume fraction profile peak is much closer to the pipe wall than is the bubble volume fraction peak.

4. Conclusions

Expanded polystyrene particle and oil two-phase flows in a vertical pipe were investigated using the three-dimensional PIT method. Particle volume fraction profiles and other flow parameters were measured for particle–liquid flows with different particle sizes in order to study particle size effects.

The experimental results show that particles in both the large and small particle–liquid flows have wall-peaked distributions although the large particle size was 5.4 mm. Furthermore, most of the particles contact the pipe wall and have a sliding-colliding motion if the liquid superficial velocity is higher than 0.24 m/s for large particle flows or 0.15 m/s for small particle flows. Results also showed that particles in high velocity flows tend to line up to form particle clusters. As liquid velocity decreases, transition from the ordered particle distribution structure consisting of the particle clusters to the random distribution occurs.

The particles have almost the same distribution as spherical bubbles in real bubbly flows. The major difference in phase distribution between real bubbly flows and the particle liquid flows may result from the deformation of bubbles. Bubble deformation generates a smaller lift force and possibly a larger wall repulsion force, which makes the bubble volume fraction profile peak shift toward the pipe center and even produces a pipe center-peaked bubble volume fraction profile.

The wall shear stress in particle–liquid flows is much larger than in real bubbly flows due to the particle–wall collision and the highly wall-peaked particle volume fraction profile.

References

Alajbegovic, A., Assad, A., Bonetto, F., Lahey Jr., R.T., 1994. Phase distribution and turbulence structure for solid/fluid upflow in a pipe. Int. J. Multiphase Flow 20, 453–479.

Bagchi, P., Balachandar, S., 2002. Effect of free rotation on the motion of a solid sphere in linear shear flow at moderate Re. Phys. Fluids 14, 2719–2737.

Cuenot, B., Magnaudet, J., Spennato, B., 1997. The effects of slightly soluble surfactants on the flow around a spherical bubble. J. Fluid Mech. 339, 25–53.

Ervin, E.A., Tryggvason, G., 1997. The rise of bubbles in a vertical shear flow. J. Fluids Eng. 119, 443–449.

Kashinsky, O.N., Timkin, L.S., Cartellier, A., 1993. Experimental study of "laminar" bubbly flows in a vertical pipe. Exp. Fluids 14, 308–314.

Kariyasaki, A., 1987. Behavior of a gas bubble in a liquid flow with a linear velocity profile. Transactions of JSME, Series B 53, 744–749 (in Japanese).

Kurose, R., Komori, S., 1999. Drag and lift force on a rotating sphere in a linear shear flow. J. Fluid Mech. 384, 183–206.

Luo, R., Song, Q., Yang, X.Y., Wang, Z., 2002. A three-dimensional photographic method for measurement of phase distribution in bubbly flows. Exp. Fluids 32, 116–120.

Lucas, D., Krepper, E., Prasser, H.M., 2001. Prediction of radial gas profiles in vertical pipe flow on the basis of bubble size distribution. Int. J. Therm. Sci. 40, 217–225.

Nakoryakov, V.E., Kashinsky, O.N., Randin, V.V., 1996. Gas–liquid bubbly flow in vertical pipes. J. Fluid Eng. 118, 377–382.

Oesterlè, B., Bui Dinh, T., 1998. Experiments on the lift of a spinning sphere in a range of intermediate Reynolds numbers. Exp. Fluids 25, 16–22.

Pan, X.H., Luo, R., Yang, X.Y., Yang, H.J., 2002. Three-dimensional particle image tracking for dilute particle liquid flows in a vertical pipe. Meas. Sci. Technol. 13, 1206–1216.

Rivière, N., Cartellier, A., Timkin, L., Kashinsky, O., 1999. Wall shear stress and void fraction in Poiseuille bubbly flows: Part II: experiments and validity of analytical predictions. Eur. J Mech. B/Fluids 18, 847–867.

Sankaranarayanan, K., Sundaresan, S., 2002. Lift force in bubbly suspensions. Chem. Eng. Sci. 57, 3521–3542.

Spelt, P.D.M., Sangani, A., 1998. Properties and averaged equations for flow of bubbly liquids. Applied Research 58, 337–386.

Song, Q., Luo, R., Yang, X.Y., Wang, Z., 2001. Phase distribution for upward laminar dilute bubbly flows with non-uniform bubble sizes in a vertical pipe. Int. J. Multiphase Flow 27, 379–390.

Tomiyama, A., Tamai, H., Zun, I., Hosokawa, S., 2002. Transverse migration of single bubbles in simple shear flows. Chem. Eng. Sci. 57, 1849–1858.